Energy response of ISS-CREAM calorimeter with attenuation effect

H.G. Zhang[a], D. Angelaszek[a,b], M. Copley[a], J.H. Han[a], H.G. Huh[a], Y.S. Hwang[c,e], H.J. Hyun[c,h], K.C. Kim[a], M.H. Kim[a], H.J. Kim[c], K. Kwashnak[a], M.H. Lee[a,d,**], J. Lundquist[a], L. Lutz[a], A. Malinin[a], H. Park[c], J.M. Park[c,f], N. Picot-Clemente[a], E.S. Seo[a,b,**], J. Smith[a], J. Wu[a], Z.Y. Yin[a], Y.S. Yoon[a,g]

[a] *Institute for Physical Science and Technology, University of Maryland, College Park, MD 20742, USA*
[b] *Department of Physics, University of Maryland, College Park, MD 20742, USA*
[c] *Department of Physics, Kyungpook National University, Daegu 41566, Korea*
[d] *Center for Underground Physics, Institute for Basic Science (IBS), Daejeon 34126, Korea*
[e] *Korea Atomic Energy Research Institute, Gyeongju 38180, Korea*
[f] *Advanced Radiation Technology Institute, Korea Atomic Energy Research Institute, Jeongeup 56212, Korea*
[g] *Korea Research Institute of Standards and Science, Daejeon 34113, Korea*
[h] *Pohang Accelerator Laboratory, Pohang 37673, Korea*

Abstract

The NASA mission, Cosmic Ray Energetic And Mass experiment for the International Space Station (ISS-CREAM) is to measure individual cosmic-ray particle energy spectra from protons to iron nuclei, with an energy range from 1 TeV to the so-called "knee", near 10^{15}eV. Energies of cosmic-ray particles are measured from electromagnetic showers induced by particles in the calorimeter.

As a pioneer mission, the balloon-borne CREAM instrument has successfully flown seven times over the Antarctica for a cumulative exposure of 191 days. The CREAM calorimeter has shown sufficient capability to measure energies of cosmic-ray particles by capturing the electromagnetic shower profile within the interested energy range. The ISS-CREAM calorimeter is expected

*Corresponding author: mhlee@ibs.re.kr
**Corresponding author: seo@umd.edu

to have a similar performance and, before it was launched, an engineering-unit calorimeter was shipped to CERN for a full beam test. The full performance test includes position, energy, and angle scans of electron and pion beams together with a high voltage scan for calibration and characterization.

In addition to the regular analysis for performance test, we also applied an additional step to generate the universal energy responses by correcting the attenuation effect in the calorimeter readout. The general energy responses could be obtained after shifting the incident beam positions to a reference position near the center of the calorimeter, which provided improved energy resolutions. The result of this analysis will be used to determine the incident energies of the cosmic-ray particles in the flight data.

Keywords: ISS-CREAM, cosmic rays, calorimeter, calibration, energy response, attenuation

1. Introduction

Understanding the origin, acceleration and galactic propagation of cosmic rays is a hot research topic in astroparticle physics. The observed "knee" structure in the all particle spectrum is related to the mechanism of acceleration, propagation, and confinement. The balloon-borne experiment CREAM [1] and its successor ISS-CREAM [2] were designed to directly measure the charges and energies of cosmic-ray nuclei, from protons to Irons, for energies ranging from a few hundred GeV to over 1 PeV, covering the "knee".

In August 2017, the ISS-CREAM payload was launched and finally deployed on the International Space Station, and in February 2019, the ISS-CREAM instrument has finished its mission, with 546 days of data collected and to be analyzed (more details can be found in [3]). Before the launch, an ISS-CREAM engineering-unit instrument, a copy of the flight unit, was taken to the European Organization for Nuclear Research (CERN) and exposed to electron and pion beams for calibration and performance tests. We report the analysis results of the calibration test in this paper.

The ISS-CREAM instrument consists of a few more sub-detectors including especially the silicon charge detector (SCD) [4, 5] and the top and bottom counting detectors (T/BCD) [6, 7] in addition to the calorimeter(CAL) [8]. The SCD comprises of four layers of pixelated silicon sensors to measure the charges of incoming nuclei independently. The CAL has twenty layers of tungsten and scintillating fiber ribbons to trigger events and measure the en-

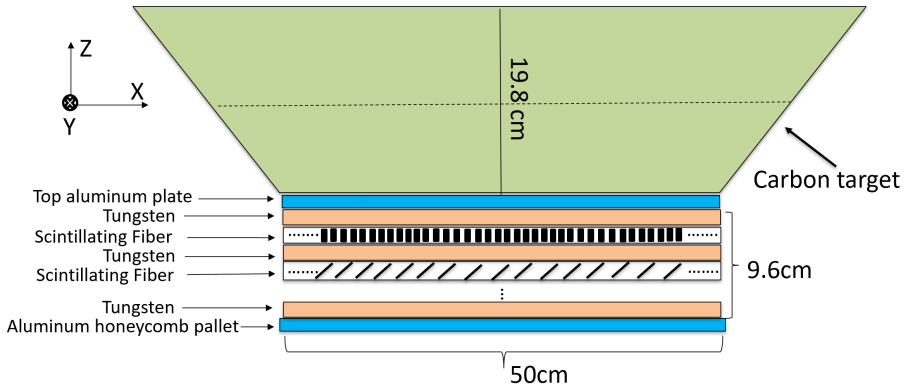

Figure 1: A cross-section view of the calorimeter and the carbon target. The calorimeter is constructed with 20-layers of tungsten plates and 1000 scintillating fiber ribbons in 20 layers.(not to scale)

ergies of the particles. The T/BCD is used for an electron/proton separation and as a redundant trigger system.

As a sampling calorimeter, the ISS-CREAM calorimeter is designed to measure mainly the electromagnetic shower component of the nuclei-induced hadronic interaction in the upper densified-graphite target. On each ribbon with nineteen 0.5 mm diameter scintillating fibers, the scintillation lights generated by charged particles in the shower is transmitted to a hybrid photodiode (HPD) via a light mixer and a bundle of clear fibers. The light signal is divided into three different sub-bundles, low, mid, and high ranges by different numbers of clear fibers (42, 5, and 1 respectively). Combining the three optical sub-ranges gives enough dynamic range to cover energies of the measured cosmic-ray particles.

After conversion of the photons as photo-electrons in the photo-cathode of the HPDs, the photo-electrons accelerated between the photo-cathode and a pixelated diode create electron-hole pairs. The pairs are read out by a charge amplifier and then sent to both a fast-shaping circuit for a trigger and a slow-shaping circuit to be digitized with an analog to digital converter (ADC) chip (more details can be found in [9]). Fig. 1 shows a cross section view in $[X, Z]$ plane of the calorimeter stack on top of an aluminum honeycomb pallet with a total height of 9.5cm, preceded by a densified-graphite target. The calorimeter is composed of twenty 3.5 mm thick 50 cm $\times$ 50 cm tungsten plates, corresponding 20 radiation length(X_0), which serve as the passive medium.

Between each of two consecutive tungsten layers is a layer with fifty fiber ribbons. While a half of the fiber ribbons, which is every other ribbons, are mated with light guides on one side of the calorimeter, the other half are mated on the opposite side. The area covered by the fiber ribbons on the layer is the same as that by tungsten plate. The dimensions of the fiber ribbon are 1 cm $\times$ 50 cm with the effective thickness of 0.64mm including a glue to combine nineteen fibers. The fiber ribbons placement pattern is shown in Fig.2.

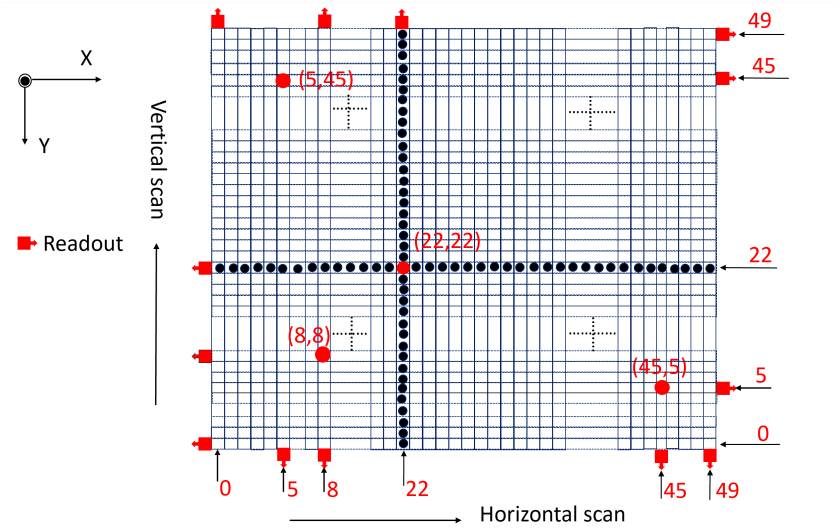

Figure 2: Part of the first two-layers of the calorimeter ribbon layout, and position scan illustration. One layer with ribbons aligned vertically is exposed to beams on horizontal scan beam positions by moving in X direction, while the other layer with ribbons aligned horizontally is exposed to beams on vertical scan beam positions by moving in $\pm$Y direction. The black points represent the incident electron beam spots. The beam crossing points are located at $[22, 22]$ in $[\mathrm{X}, \mathrm{Y}]$ plane, and there are 20 crossing points in total layers. The beam scans at positions with red circles are considered in section 6.5.

In order to make the detector comply with the rocket-launch requirements, a bracket is clamping them down on each side to maintain the fiber ribbon and tungsten plates in their fixed positions. Also, a stainless steel wire of 1.02 mm thickness (0.9 mm used for the balloon units) for each layer to maintain a gap between tungsten plates and fiber ribbons. Moreover, for light-tightness and maintenance of the calorimeter stack, epoxy-coated fiberglass sheets (Tedlar sheets by Dupont were used in the balloon units) were added between the plates and fiber ribbons for a better protection during

the rocket-launch process.

The beam test at the CERN's Super Proton Synchrotron (SPS) experimental site offered an opportunity to calibrate the instrument using electron beams up to 175GeV and pion beams up to 350GeV. The engineering unit made of graphite target and calorimeter module was installed in the CERN SPS north area to characterize its performance and for calibration.

In this paper, the calorimeter responses to electron and pion beams are studied. Section 2 is a detail description of the position scan using electron beams, as well as a general introduction to the data processing. In section 3, we show how to correct the attenuation effect on each ribbon, and how to generate an universal deposited energy. Section 6 is the study of the energy response to electron and pion beams. The last section is a conclusion of this study.

2. Electron position scan

Aiming at measuring the electromagnetic shower components of the cosmic-ray particles, the detector initiates the hadronic showers upstream of the calorimeter with two light blocks of densified graphite with a density of 1.92 g/cm^3 and a total thickness of 19.75cm as a target. A significant portion of the electromagnetic shower core and the shower maximum in longitudinal shower profile are contained in the tungsten/scintillating fiber ribbon layers.

The calibration of the scintillating fibers in the calorimeter is important to correctly measure and reconstruct the shower energies of the incident particles. Position scan is used to measure responses of all the 1000 fiber ribbons (50 ribbons $\times$ 20 layers) in the calorimeter with beams coming downstream on the calorimeter.

In the position scan, we used an electron beam of 150 GeV with a beam profile diameter of about 0.6 cm from the beam trigger counter size of 2 cm $\times$ 2 cm to calibrate the readout channels of the fiber ribbons. As shown in Fig. 2, ribbons numbered 22 (the 22nd ribbons from -X or -Y side) of odd layers in the calorimeter were exposed to beams for the vertical scan. Then, after collecting enough data, the calorimeter was moved by 1 cm along Y direction to place the next ribbon center exposed to the beams. Position adjustment and measurement were repeated for all fifty ribbons in the odd layers. In the same way, the calorimeter was moved by 1 cm along X direction to place all the ribbon center of even layer to the beams for the horizontal scan.

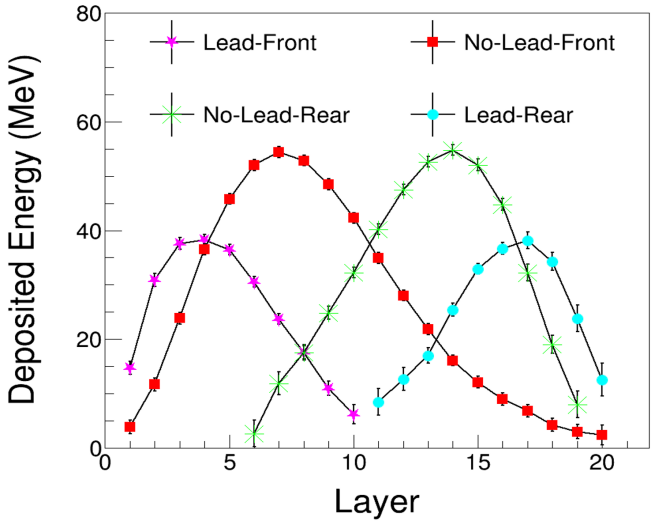

Figure 3: Deposited energy per fiber ribbon from Monte Carlo (MC) simulation results using 150 GeV electron beams. We perform position scan with electron beams at four detector configurations in the beam line, "No-Lead-Front", "No-Lead-Rear", "Lead-Front", and "Lead-Rear", in order to place shower maximum positions from top to bottom of the calorimeter evenly.

2.1. Four detector configurations for position scan

The calorimeter with carbon target was mounted on a rotation fixture, placed on a moving table in the beam line, and rotated to get 90° between the incident beams and the [X, Y] plane. In order to get enough electromagnetic shower particles in each layer and place shower maximum positions throughout the layers, the four detector configurations for vertical and horizontal position scans were implemented. Details are explained as below.

In "No-Lead-Front" scan, the electron beam was injected in front of the graphite target to get a detector response from the electron shower particles passing through ribbons in the middle layers. The "No-Lead-Rear" scan is similar, however the electron beam was then injected with the instrument rotated so that the electron beam was incident on the bottom.

In the "Lead-Front" scan, two of 2.5 cm thick lead bricks were placed in front of the graphite target to place the shower maximum in the first few layers where the showers have not been initialed in previous two configurations. The "Lead-Rear" scan is similar, however, the lead bricks were placed when instrument rotated to calibrate the bottom layers. In addition, two tung-

sten plates were placed between the honeycomb pallet and the lead bricks to compensate for the two missing radiation lengths of the carbon target.

We performed the Monte Carlo (MC) simulations with an equalization process for the four detector configurations in position scans to convert a response in ADC count unit on each ribbon to the deposited energy in the MC data. The longitudinal shower profiles per fiber ribbon in each layer in the four configurations are shown in Fig. 3. Following those profiles, to receive enough shower particles in each layer, we calibrate the top four and bottom four layers using the data from "No-Lead-Front" and "No-Lead-Rear" scans, while for layers 5-10 and 11-16, we use the data from "Lead-Front" and "Lead-Rear" scan, respectively.

2.2. Data processing

Data processing which converts the raw beam data to the calibrated data is outlined in Fig.4. The calibration factors are generated by comparing the measured signal in the beam data with that of the deposited energy in the MC data on each ribbon. We measured the raw signals in ADC count unit after the pedestal subtraction and rejecting hadronic events contaminated in electron beams while the corresponding deposited energies in the MC data are obtained with smearing for electronics noise and photon statistics.

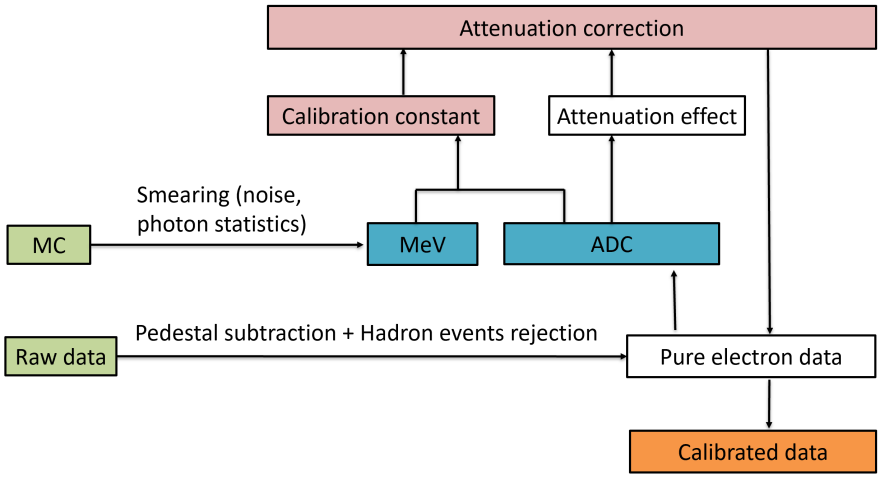

Figure 4: A diagram for data processing in the calibration.

In section 4, the attenuation effect is considered and the correction factors are generated on each ribbon. We show how to correct the attenuation effect

in section 5, and based on that, we generate the universal energy responses for electron and pion beams in sections 6.1-4.

3. Calibration constant and attenuation effect

The first step in calibration of the ISS-CREAM calorimeter is to determine calibration constant of each ribbon. Based on identifying each event having the maximum on the fiber ribbon, the calibration constant in MeV/ADC unit is obtained by a ratio of two values [6]. The one is the distribution of the maximum deposited energy on a fiber ribbon in MeV unit from the MC simulation results. The other is the distribution of the maximum signal in ADC count unit on each fiber ribbon from beam response measurement.

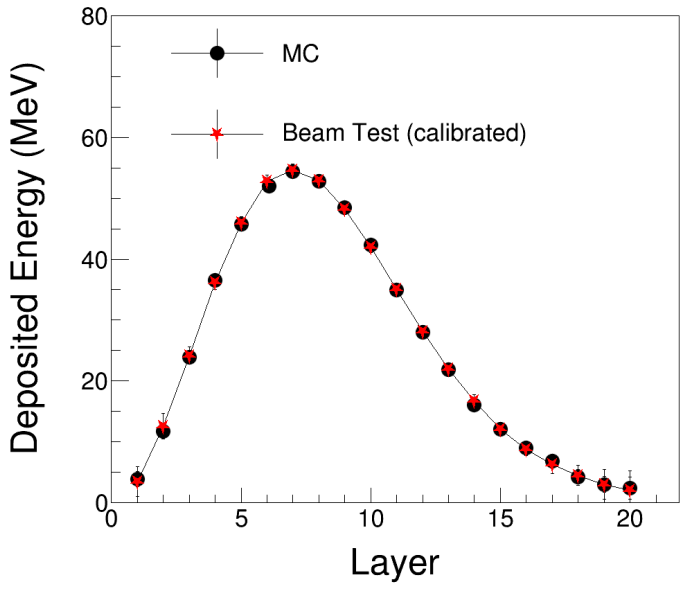

Figure 5: An excellent agreement between deposited energies of all layers from calibrated data and that from MC simulation is shown. We measured the deposited energy from the calibrated data with 10-time repeated beam test data at $[22, 22]$ in $[\mathrm{X}, \mathrm{Y}]$ plane.

Although the incident beam spot is known with respect to the fiber ribbon number and physical position, particles in the shower can hit the neighboring fiber ribbons, because not only the shower has lateral shower profile but also

the beam width is wider than width of a ribbon width, 1cm. Only those events where the fiber ribbon nominally "in the beam" actually records the maximum are selected. In order to select the appropriate events, we also implemented a pre-selection cut to subtract the hadronic events from the contaminated hadron particles (i.e., pions).

We calibrated the 1000 fiber ribbons and plotted the longitudinal shower profiles with electrons in Fig. 5. As we expected, the deposited energies from the calibrated data agree perfectly with the deposited energies from the simulation data.

4. Attenuation effect and attenuation length

As scintillation lights, originated from shower particles of an incident particle inside the calorimeter, pass through a fiber ribbon, they interact with the material and getting weaker. Suppose intensity of the signal at the origin is I_0, a good approximation for the intensity at position x passing through the fiber ribbon decreases exponentially with length in a form of $I(x) = I_0 \times e^{-x/\lambda}$, where λ is the attenuation length and x is the distance from the readout. We denote ribbon number 22 in both odd and even layers as beam ribbons with hits, where the electron beam injected and developed electromagnetic showers along the layers.

The correction factors of different ribbons in each layer are shown in Fig. 6. From the data, we estimated the attenuation length values of ribbons in each layer by fitting with the attenuation function. As shown in Fig. 7, the distribution of the attenuation length values for different ribbons in 20 layers shows a Gaussian distribution, and the most probable value of the attenuation length is found to be 195cm (the mean value is fitted to be 195 cm while the σ is fitted to be 3.14), which implies the intensity of the signal drops to around 1/5 when it passes through the whole ribbon length of 50 cm. In addition to that, because the attenuation length values of twenty different ribbons are given in a Gaussian distribution, it can be assumed the rest ribbons have the same trend. In this paper, we applied this most probable attenuation length to all the 1000 ribbons in the calorimeter.

It is convenient to denote $\Delta(x) = I(x)/I(x_c) = e^{-(x-x_c)/\lambda}$ as the correction factor, where $I(x_c)$ is the beam data value at the crossing point [22, 22]. In fact, the correction factor is the relative signal value of each beam point compared to that at the crossing point and the attenuation effect at each beam point can be corrected directly. In section 5, we explain why we normalize

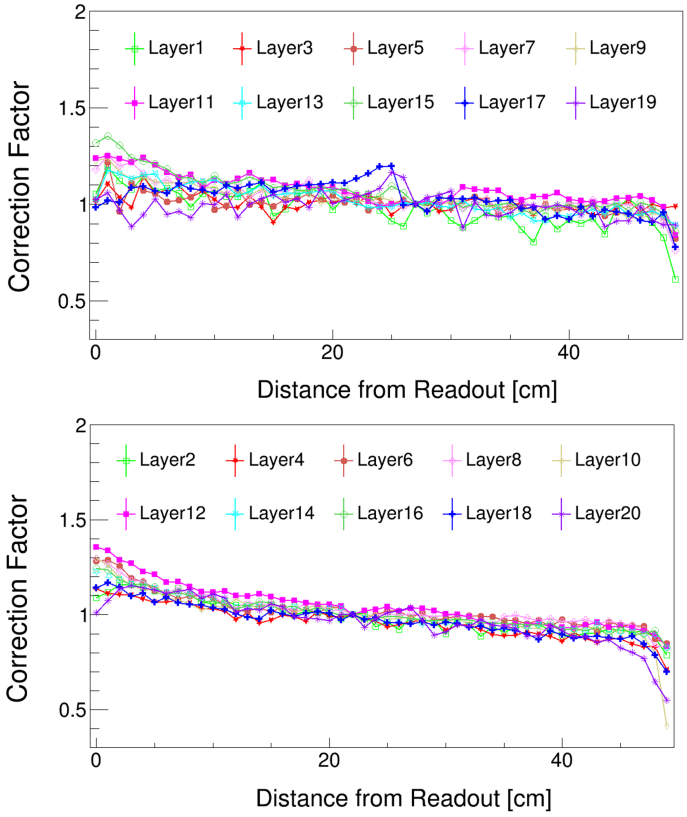

Figure 6: The correction factors for ribbons in odd layers(top) and even layers(bottom).

the signal value at crossing point and how to generate the correction factors for all the 50,000 beam points (50 beam positions on each ribbon and 1000 ribbons in the calorimeter) with a proper attenuation length.

5. The strategy for universal energy response

The ultimate goal of the calibration is to determine the sampling fraction of the deposited energy to the incident energy of a cosmic particle. However, as shown in section 4, the deposited energy is changed by the incident position due to the attenuation effect. How to construct an universal energy response after correcting the attenuation effect is what we are going to devote in this section.

First, for a particle with fixed incident energy and fixed incident position, the correction factor gives us an opportunity to determine the raw signal

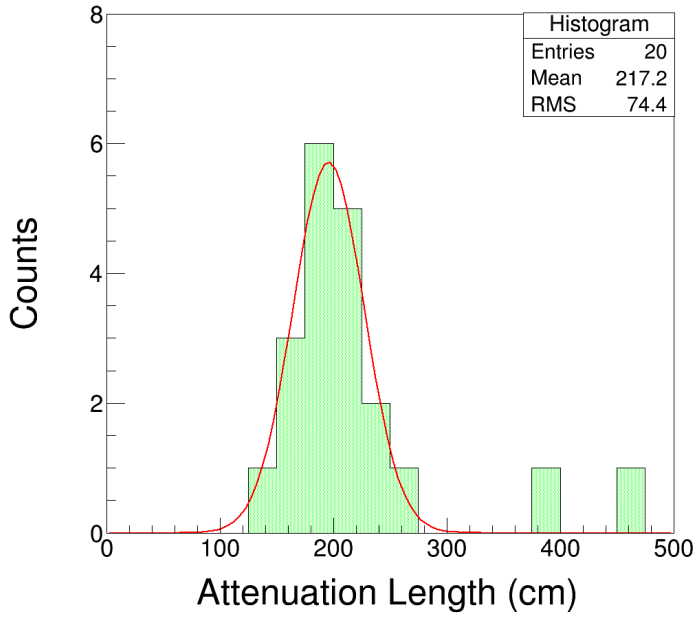

Figure 7: The distribution of attenuation lengths in twenty ribbons from 20 layers.

intensity at any given positions.

Second, it is clear that the ribbons with beam hits in all layers are calibrated by the "real" beam in position. In our four detector-configurations for position scans, only the ribbons at the crossing point are calibrated by the "real" beam while there are no attenuation effects. This implies the energy response at this point is universal.

Thus, we can correct the measured signal I(x) at any incident beam positions by "shifting" it to the crossing point (the reference position) to avoid the attenuation effect. In this way, the measured signals in even layers and old layers at the crossing points are given by $I(x_c) = I(x)/\Delta(x)$ and $I(y_c) = I(y)/\Delta(y)$. From the definition, the deposited energies on even and odd layers are given by

$$\begin{aligned} E(x_c) &= I(x_c) \times \delta(x_c) = I(x)/\Delta(x) \times \delta(x_c) \\ E(y_c) &= I(y_c) \times \delta(y_c) = I(y)/\Delta(y) \times \delta(y_c). \end{aligned} \quad (1)$$

Here the deposited energies $E(x_c)$ and $E(y_c)$ are not dependent of incident positions. In section 6.1 and 6.2, we apply this method to generate the universal deposited energies for electron and pion beam scan data.

5.1. The variation and stability of ribbon response

We were aware that the intensity of the signal at each ribbon in a layer are different because each ribbon has different light-output and high-voltage gain. As an example as shown in Fig. 8 (top), the maximum variation from ribbon to ribbon is about 400 ADC count in layer 8. This variation in the ribbon response of raw signal distribution in ADC unit was corrected by the calibration constant when each signal in ADC count unit was properly converted to the energy deposit in MeV unit. In order to avoid confusion, the attenuation effect and correction of the signal in previous sections are correction for the position difference on the same ribbon.

Also, we confirmed that signal responses in the same position have a good stability for repeated measurements. As shown in Fig. 8 (bottom), the distribution of the responses with 10 repeated measurements at the crossing point in layer 8 shows a narrow Gaussian distribution (the fitted mean value is 561 and the fitted σ is 0.68), which means the ADC value measured at the crossing point is stable. Furthermore, this implies that the signal response variations on different ribbons in certain layer are not caused by the statistics but are determined by the property of the fiber ribbon itself.

5.2. The pedestal value

We illustrated the pedestal mean values of low range for each ribbon in Fig. 9. They are signals of randomly triggered events by a calibration system without electron beam signals (by an active veto of the beam triggered events) during the electron position scan in all four detector configurations. Since a 16-bit ADC chip was used, the readout range is from 0 to 65535 ADC counts and the pedestal level was set at the middle, $\sim$32767 ADC count. This is because we want to enable the temperature compensation in the charge amplifier chip by not having a biased reference voltage output to accommodate the temperature variation in the flight environment expected. For ribbons in one layer, the values vary by about 3000 ADC, which is about 5% of readout range. The variation doesn't any affect much because not only the charge amplifier input does not saturate the ADC but also there are three optical sub-ranges, low, middle, and high-ranges for each ribbon readouts. The signal at the mid/high range is used when a signal in the low/mid range is saturated. More details can be found at the instrument paper.

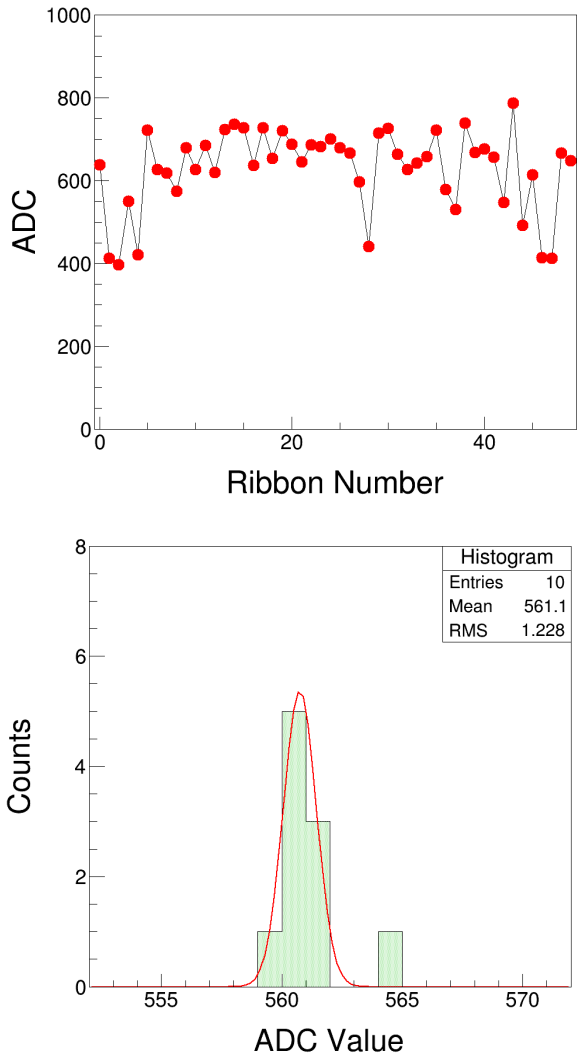

Figure 8: The signal response of ribbons in ADC unit with beam hits in layer 8 (top). Distribution of the signal response on ribbon 22 in layer 8 (bottom) with 10-time repeated measurements at $[22, 22]$ in [X, Y] plane.

6. The energy response and resolution

After obtaining the calibration contants from the electron position scan data, we studied the electron energy scan, the pion energy scan, the angle scan and the high voltage scan in section 6.1-4 to characterize the energy

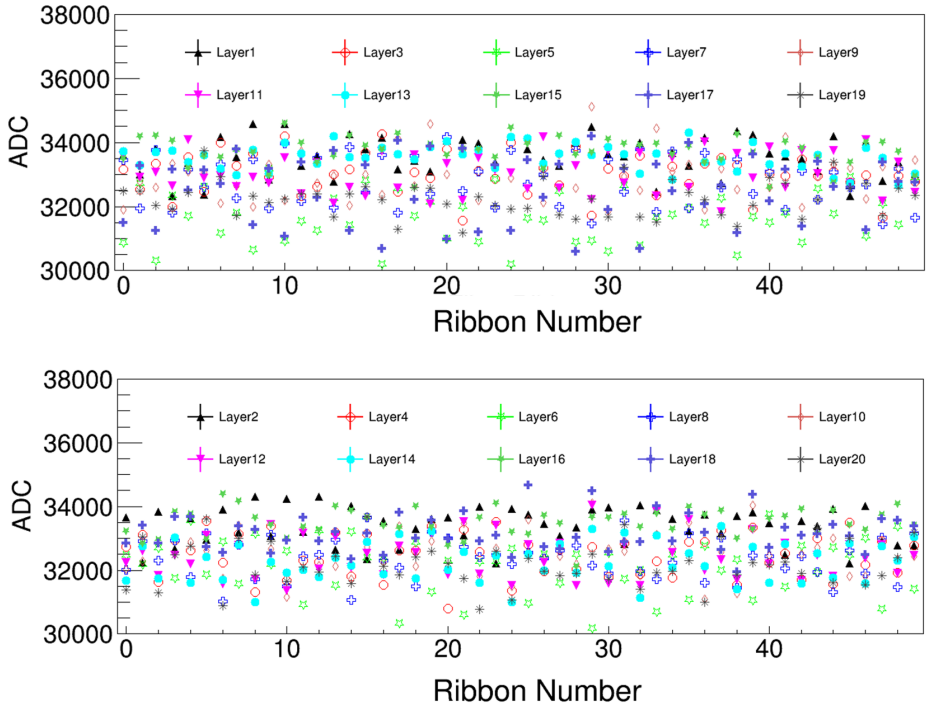

Figure 9: The pedestal mean values for ribbons in odd layers(top) and even layers(bottom).

responses of the calorimeter. In section 6.5, we explain how the energy responses changed by the attenuation corrections. In section 6.6, we check if the energy of the primary particle has fully deposited in the calorimeter. The energy responses generated in the section is taken from the "No-Lead-Front" beam scan. The incident beam position is fixed at $[8, 8]$ (see Fig.2) in $[X, Y]$ plane for electron energy scan and pion energy scan, while for angle scan and high voltage scan, the incident position is fixed at $[36, 36]$ in $[X, Y]$ plane.

6.1. The electron energy scan

We performed the electron beam scan with energies varying from 50GeV to 175GeV with a purity of 95% to characterize the energy response of the calorimeter. Though the use of electron beams brings a relatively clean signal in the detector, hadron particles in the electron beams are still found to be contaminated. We performed a pre-selection with a cut on sum of five neighboring fiber ribbons and layers to remove the hadronic events.

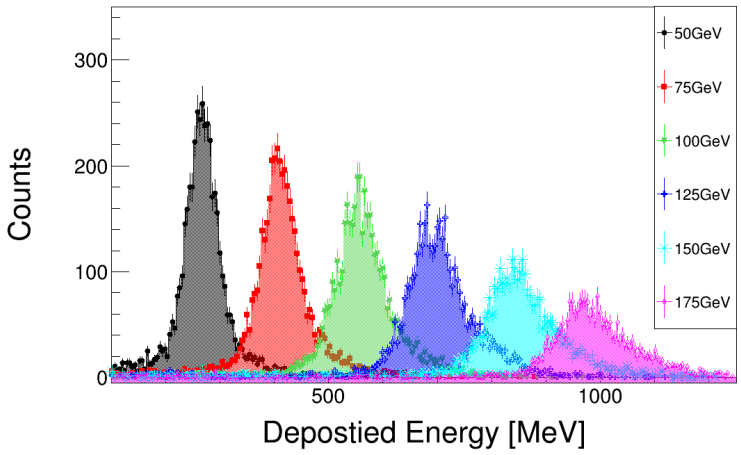

Figure 10: Calorimeter responses of energy deposits from incident electron beam energies of 50, 75, 100, 125, 150, and 175 GeV after calibration and attenuation correction.

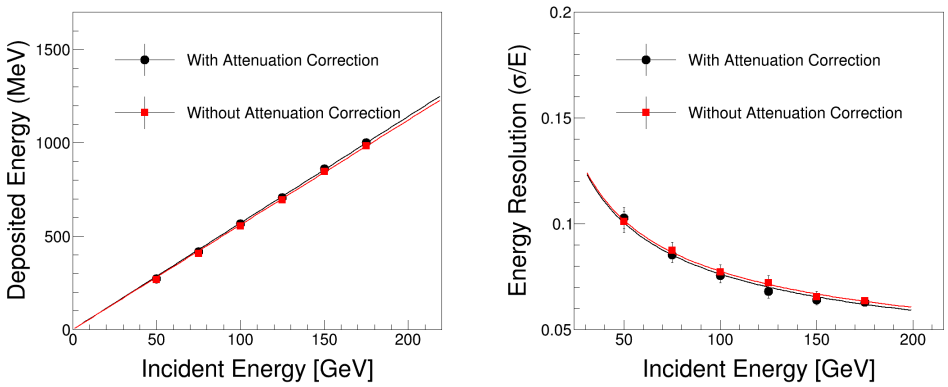

Figure 11: Mean energy deposit in the calorimeter as a function of the incident electron beam energies (left). Energy resolution of the calorimeter as a function of the incident electron beam energies (right).

After applying calibration and the attenuation correction, the deposited energy distributions from various incident energy electron beams are shown in Fig. 10. Gaussian function fits are used to determine the mean energy deposits in the detector. The energy response of the calorimeter as shown in Fig. 11 (left) proves to be linear with increasing incident electron beam

energies, with the slop fitted to be 5.70MeV/GeV, or the sampling fraction of the deposited energy to the incident energy is 0.57%. The deposited energy with 150 GeV incident beam is fitted to be 850 MeV, and we find the sampling fraction changed (enhanced) by the attenuation correction is about 1%.

As shown in Fig. 11 (right), the energy resolution with respect to the incident electron beam energy is fitted by using the quadratic function with a constant term, $\sigma_{\mathrm{E}}/\mathrm{E} = 0.586/\sqrt{\mathrm{E(GeV)}} \oplus 0.018$ when considering the attenuation correction. The energy resolution is found to be 10.0% at 50 GeV and improves with increasing energy, reaching 6.60% at 150 GeV. The smaller (higher) energy resolution at higher energy is due to more number of shower particles generated in the calorimeter compared with that for lower energy electrons. For the case without attenuation correction, the energy resolution is fitted by $\sigma_{\mathrm{E}}/\mathrm{E} = 0.582/\sqrt{\mathrm{E(GeV)}} \oplus 0.019$, and at 150GeV, the resolution is 6.65%. The energy resolution improved by the attenuation correction is about 1%.

6.2. The Pion energy scan

The calorimeter aims to measure the electromagnetic component of hadronic showers induced in the preceding carbon target by high-energy interacting nuclei. We performed pion beam test with energies from 250 GeV to 350 GeV in order to characterize the energy response of the calorimeter to incident hadrons.

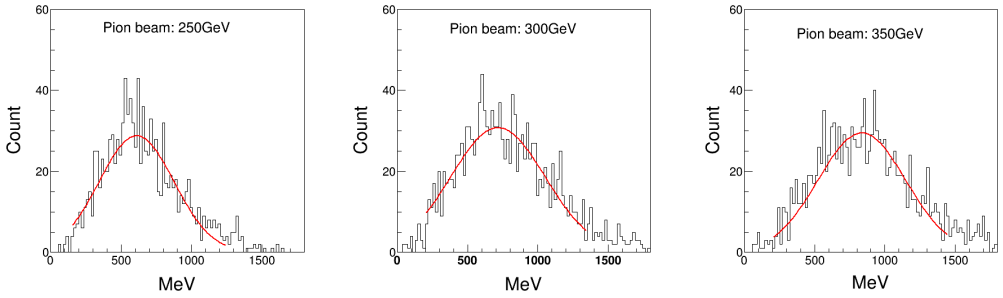

Figure 12: Energy deposits in calorimeter for pion beams with incident energies of 250 GeV(left), 300 GeV(middle), and 350 GeV(right).

In order to obtain only pions that interacted in the carbon target upstream of the calorimeter, we performed a pre-selection requiring events with enough signals in the first three layers of the calorimeter, to obtain a good

Gaussian distribution. The deposited energy distributions with summing over five ribbons and layers at the center on the beam position with different incident energies are shown in Fig. 12.

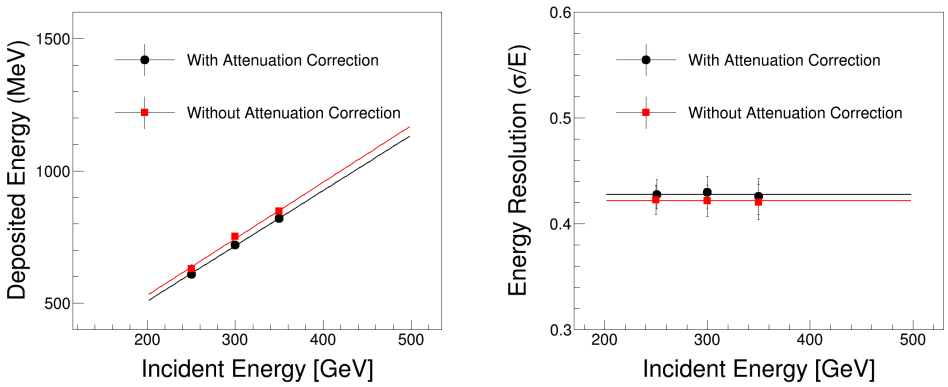

Figure 13: Mean energy deposit in the calorimeter (left) and energy resolution of the calorimeter (right) as a function of the incident pion beam energy.

As shown in Fig. 13 (left), the dependence of the deposited energy to the incident energy of pion beam is observed to be linear. After applying the attenuation correction, the sampling fraction is found to be 0.190%, which is about 1/3 of the electron beam. This is consistent with theoretical expectations that when cosmic-ray particles (mainly protons) interacting hadronically with the calorimeter, on average approximately 1/3 of the energy of the primary nuclei is converted into neutral pion π^0, which then rapidly decay into two photons with the electromagnetic showers produced [10]. The sampling fraction without attenuation correction is fitted to be 0.192%.

The dependence of energy resolution with incident energy for pion is shown in Fig.13 (right), where the resolution doesn't change much from 150 GeV to 350 GeV, with an average value of about 42.7% for pions with normal incident beams. The energy resolution without attenuation correction is about 42.2%.

6.3. The electron angle scan

The cosmic-ray particles incident into the detector from various angles in space with a good approximation of isotropic. We did angle scan to characterize the angular response of the calorimeter. Measurement of electron beam

at fixed energy of 150 GeV were performed with three different incident beam angles of 0°, 30° and 45°.

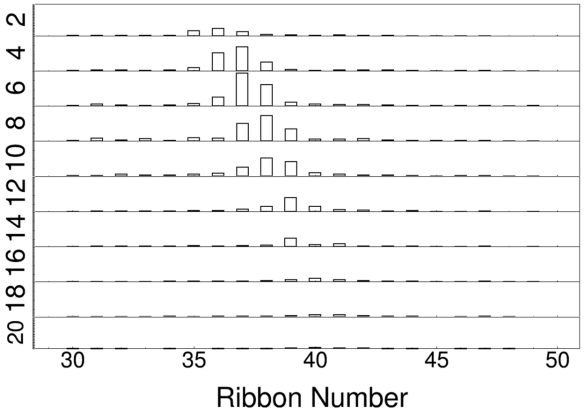

Figure 14: An event display example of ADC response of ribbons in X direction (even layers) using 150GeV electron beam with incident angle of 30°. The height of the rectangle represents the ADC value of each ribbon.

The ADC response of ribbons for angle scan is shown in Fig. 14 in X direction. The pattern represents the electromagnetic shower from a electron beam with energy of 150 GeV with incident angle of 30°. We see the electrons traverse the whole detector and produce showers with energy deposited in each layer.

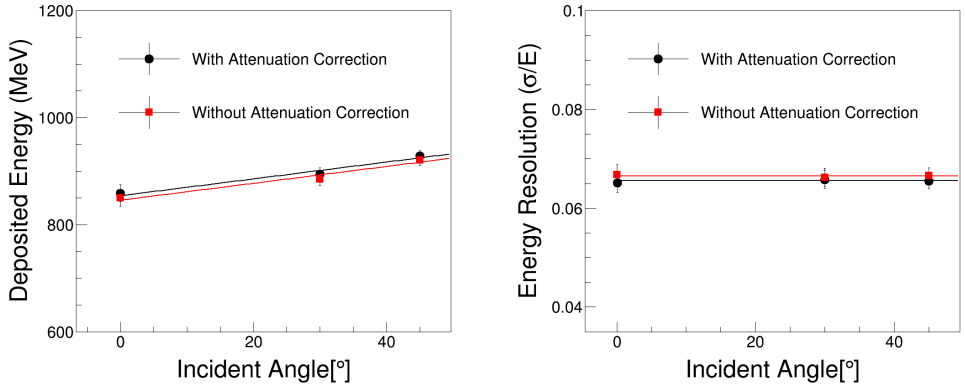

Figure 15: Mean energy deposit in the calorimeter (left) and energy resolution (right) as a function of the incident angles using 150GeV electron beam.

After applying the attenuation correction, in Fig. 15 (left), we illustrated an energy dependent function of deposited energy with increasing incident energy by fitting with a linear function with slope of 1.57 MeV/° (the fitting function is $1.57 \times \mathrm{A} + 854$ where A is the angle), about 70 MeV increases from 0° to 45°. The deposited energy at 0° is found to be 854 MeV which is consistent with what we observed in section 6.1. From Fig. 15 (left), we see that the energy response changed by the attenuation correction is about 1% (the fitting function is $1.58 \times \mathrm{A} + 845$).

The deviation of deposited energy with angles for 150 GeV electrons is about 7%. The deviation by angles at the energy of TeV can be estimated using Monte Carlo simulations since test beams with energy over TeV are not available for detector calibration. The energy resolution shown in Fig. 15 (right) changed by attenuation correction is about 1%, while it is stable at 6.65% which is consistent with the energy scan result in section 6.1.

6.4. The High Voltage scan of electron beam

The calorimeter energy response with respect to the applied high voltage (HV) of the HPD is studied in this section. This test was necessary for calibration of a calorimeter on a balloon-borne CREAM experiment, which used different HV setting vales of the HPD during the flight at the altitude of ∼40 km in order to avoid damages from corona discharges compared to those set at the beam calibration. For the calorimeter on the ISS-CREAM, the HV setting values of the HPD is the same values to the calibration test on the ground. However, the HV scan test was performed just in case any possible situation with different HV setting values in the flight.

We used the HV gain correction in the range of $[4\ \mathrm{kV}, 10.5\ \mathrm{kV}]$ to reconstruct the deposited energy of flight data. The ADC sum with respect to the HPD high voltage was tested at fixed incident beam energy of 150 GeV by changing the HV setting values.

After applying the attenuation correction, we show in Fig. 16 (left) that the deposited energy as a function of high voltage is fitted by a linear function with a slope of 101 MeV/kV(the fitting function is $101 \times \mathrm{HV} - 180.0$). The deposited energy is fitted to be 850 MeV for 10.5 kV, which is consistent with what shown in section 6.1. The energy response changed by the attenuation correction is smaller than 2% (The fitting function is $965 \times \mathrm{HV} - 172.5$).

As shown in Fig. 11, the energy resolution of calorimeter for electron beam as a function of HV is fitted using the quadratic function $\sigma_{\mathrm{E}}/\mathrm{E(H)} = 0.188/\sqrt{\mathrm{HV(kV)}} \oplus 0.0067$. We observe that the energy resolution at 10.5 kV

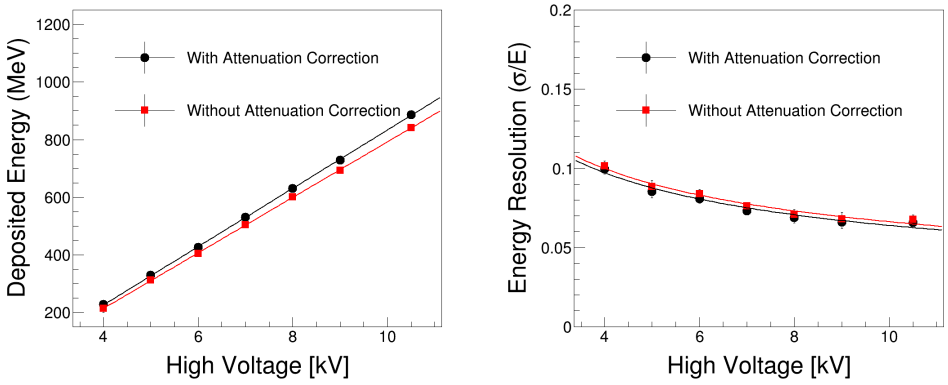

Figure 16: Mean energy deposit in the calorimeter (left) and energy resolution of the calorimeter (right) as a function of the high voltages using electron beam with 150 GeV.

is about 6.6%, which is consistent with the resolution(6.4%) obtained in section 6.1, where the voltage is 10.5 kV either. For the case without attenuation correction, the energy resolution is fitted by the function $\sigma_{\mathrm{E}}/\mathrm{E}(\mathrm{H}) = 0.185/\sqrt{\mathrm{H(kV)}}\oplus 0.0086$, and the value at 10.5 kV is 6.70% which is consistent with what we found from section 6.1 (6.60%).

6.5. Analysis about the attenuation correction

The energy responses shown in section 6.1-4 are measured before and after applying the attenuation correction, however, because of two reasons the energy changed by the attenuation correction is small. First, as the readouts of the neighboured ribbons in the same layer are located at different sides of the calorimeter, the energy changed by the attenuation correction is cancelled each other at some level when summing over five ribbons. Second, the incident beam positions($[8, 8]$ or $[36, 36]$) are special as the distances from the incident beam points to the crossing points ($[22, 22]$) in the neighbored layers are the same, but attenuation correction increases and decreases in the neighbored layers. Thus, the energy changed by the attenuation corrections from odd layers and even layers are canceled further.

In order to quantitatively estimate the energy responses changed by the attenuation correction at any incident position, we set up a frame below to calculate the corresponding deposited energy at any given positions using the "real" beam test introduced in section 6.1 and 6.2, and then we make a comparison of energy responses at the given positions with that from the

crossing point, where energy response is universal.

With the method introduced in section 5, we denote the "real" beam position as $[X_1, Y_1]$, and denote the given beam position as $[X_2, Y_2]$. Following Eq.(1), the deposited energies at the crossing point can be expressed as

$$\begin{aligned} E(x_c) &= I(x_1)/\Delta_{x_1} \times \delta_{x_c} \\ E(x_c) &= I(x_2)/\Delta_{x_2} \times \delta_{x_c} \\ E(y_c) &= I(y_1)/\Delta_{y_1} \times \delta_{y_c} \\ E(y_c) &= I(y_2)/\Delta_{y_2} \times \delta_{y_c}. \end{aligned} \tag{2}$$

Thus, the deposited energies in even layers and odd layers at the given position $[X_2, Y_2]$ are

$$\begin{aligned} E(x_2) &= I(x_2) \times \delta_{x_2} = I(x_1) \times (\Delta_{x_2}/\Delta_{x_1}) \times \delta_{x_c} \\ E(y_2) &= I(y_2) \times \delta_{y_2} = I(y_1) \times (\Delta_{y_2}/\Delta_{y_1}) \times \delta_{y_c}. \end{aligned} \tag{3}$$

Following the electron energy beam scan in section 6.1, we generate the energy responses in Fig. 17 at two given positions of $[45, 5]$, $[5, 45]$ (see Fig.2). In fact, what Fig. 17 showing is how the calorimeter responses to the incident energy particle with the same energy from various incident positions ($[8, 8]$, $[22, 22]$, $[45, 5]$, $[5, 45]$), while the attenuation corrections are not considered.

However, from another angle, as the energy response at $[22, 22]$ is universal, Fig. 17 (left) shows how the energy responses to the electron beams at different incident positions have been improved by the attenuation corrections, while the incident energies are the same for various cases. Quantitatively, the energy responses at $[45, 5]$ and $[5, 45]$ are decreased and increased around 10% respectively compared to the universal response at $[22, 22]$, while the energy response at $[8, 8]$ is slightly changed due to the reason we mentioned in the first paragraph of this section. The energy responses of pion beam is shown in Fig.17 (right). Compared to the universal energy response at $[22, 22]$, the energy response at $[45, 5]$ and $[5, 45]$ are 5.12 MeV/GeV and 6.3 MeV/GeV without attenuation correction.

6.6. Longitudinal shower profile in the calorimeter

For the beam energy scans introduced in 6.1 and 6.2, the longitudinal shower profiles of 100 GeV electron beam and 300 GeV pion beam are shown in Fig. 18 with respect to layer number by summing over the neighboring five ribbons. As the sampling fraction of pion beam is about 1/3 of the electron

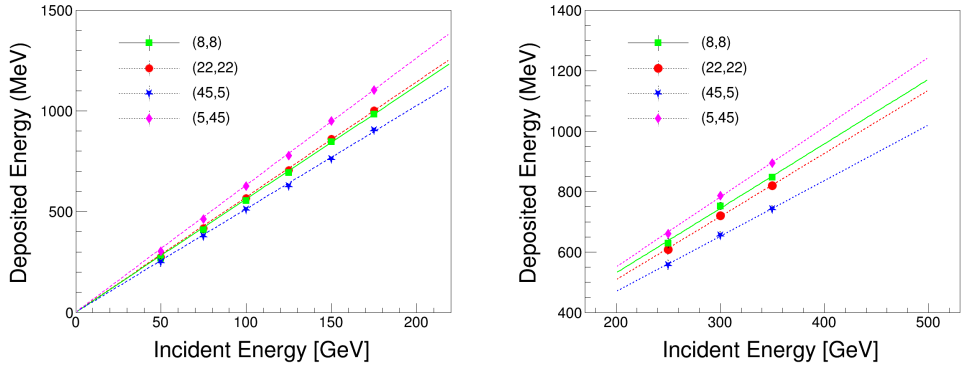

Figure 17: The energy responses for electron beams (left) and pion beams (right) with incident beams at positions of $[8, 8]$, $[22, 22]$, $[45, 5]$ and $[5, 45]$. The beam at incident position of $[8, 8]$, which is drawn with solid line, is the "real" beam, while the other three with dashed lines are the supposed beam.

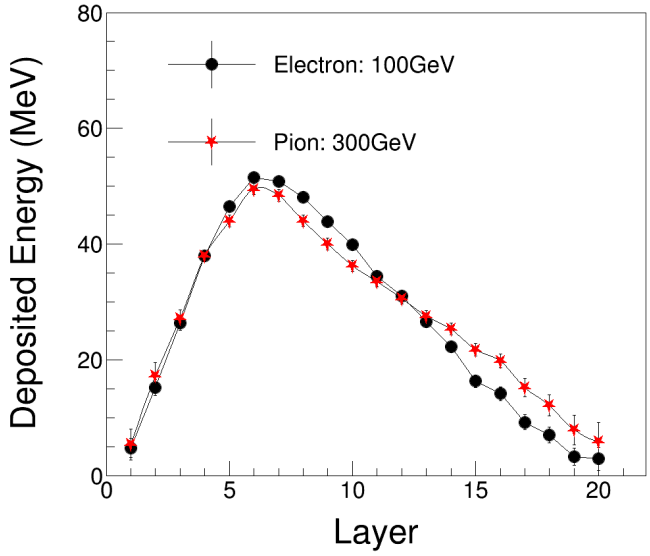

Figure 18: The energy deposit in the calorimeter summing over five ribbons in each layer for electron beams and pion beams. We measured the deposited energy from the calibrated data with 10-time repeated beam test at $[8, 8]$ in $[\mathrm{X}, \mathrm{Y}]$ plane after the attenuation correction has been applied.

beam, the deposited energies from 100 GeV electron beam and 300 GeV pion beam are similar.

We plot the energy responses considering the attenuation correction on each fiber ribbon. It is shown that the shower from pion beam is wider that that from electron beam, but clearly for both cases, the primary particles have fully converted their energies into scintillation light. Thus the deposited energies we introduced in section 6.1, 6.2 are fully considered in the energy response.

7. Conclusion

The ISS-CREAM experiment is aiming to measure the elemental cosmic-ray particles spectra covering the "knee". The ISS-CREAM detector launched in August of 2017 and installed on the ISS. In February of 2019, the operation of the ISS-CREAM has finished its 1.5 years mission, with tons of CREAM data collected.

The ISS-CREAM detector is designed to measure the deposited energies of the cosmic-ray particles from the electromagnetic shower through the electromagnetic sampling calorimeter. In order to characterize its performance, an engineering-unit calorimeter was calibrated at CERN using electron and pion beams before its launching. The result reported in this paper will be used at the flight data analysis to determine the energy of each primary particle.

During the calibration test, measurements with electron beams at multiple configurations were used to determine the ribbon response to different longitudinal shower profiles. A novel method is implemented to generate the universal energy responses for electron and pion beams by correcting the attenuation effect on each ribbon. Using this technique, the calibration factor for each ribbon was obtained and the calorimeter energy linearity was validated with electron and pion beams. Measurement shows an agreement with the prediction that 1/3 of the pion-induced shower energy is deposited in the calorimeter.

8. Acknowledgments

This work was supported in the U.S. by NASA grant NNX17AB41G, in Korea by National Research Foundation grants 2018R1A2A1A05022685 and 2018R1A6A1A06024970, and their predecessor grants. It was also supported

in France by IN2P3/CNRS and CNES and in Mexico by DGAPA-UNAM project IN109617. The authors thank NASA GSFC WFF and its contractors for engineering support and project management, JSC ISS Program Office for the launch support and ISS accommodation, MSFC for the operational support, and KSC and SpaceX for the launch support.

References

[1] Seo, E.S. et al., Advances in Space Research 33, 10, 1777-1785 (2004).

[2] Seo, E.S. et al., Advances in Space Research 53, 10, 1451-1455 (2014).

[3] E. S. Seo et al., 36th Int. Cosmic Ray Conf., Madison, USA, 137, 2019

[4] Park, I.H. et al., Nucl. Inst. Meth. A 570, 286-291 (2007).

[5] Lee, J. et al., Proc. 34th Int. Cosmic Ray Conf., The Hague, Netherlands, ID 693 (2015).

[6] Lee, M.H. et al., IEEE Trans. Nucl. Sci. 56, 1396-1399 (2009).

[7] Hwang, Y.S. et al., J. INST 10 (07), P07018 (2015).

[8] Hyun, H.J. et al., Nucl. Inst. Meth. A 787, 134-139 (2015)

[9] Link, J.T. et al., Proc. 34th Int. Cosmic Ray Conf., The Hague, Netherlands, ID 611 (2015).

[10] Hagiwara, K. et al., Phys. Rev. D 66, 010001 (2002).

[11] Ahn, H.S. et al., Nucl. Inst. Meth. A 579, 1034-1053 (2007).

[12] K.C. Kim et al., 36th Int. Cosmic Ray Conf., Madison, USA, 088, 2019